



# 1 Humidity changes and possible forcing mechanisms over 2 the last millennium in arid Central Asia

3 Shengnan Feng<sup>1</sup>, Xingqi Liu<sup>1\*</sup>, Feng Shi<sup>2,3,4</sup>, Xin Mao<sup>1,5</sup>, Yun Li<sup>6</sup>, Jiaping Wang<sup>1</sup>

4 <sup>1</sup> College of Resource, Environment and Tourism, Capital Normal University, Beijing 100048, China

5 <sup>2</sup> Key Laboratory of Cenozoic Geology and Environment, Institute of Geology and Geophysics, Chinese  
6 Academy of Sciences, Beijing 100029, China

7 <sup>3</sup> Georges Lemaître Centre for Earth and Climate Research, Earth and Life Institute, Université  
8 Catholique de Louvain, Louvain-la-Neuve 1348, Belgium

9 <sup>4</sup> CAS Center for Excellence in Life and Paleoenvironment, Beijing 100044, China

10 <sup>5</sup> Institute of Hydrogeology and Environmental Geology, Chinese Academy of Geological Sciences,  
11 Shijiazhuang 050061, China

12 <sup>6</sup> Qinghai Institute of Salt Lakes, Chinese Academy of Sciences, Xining 810008, China

13 *Correspondence to:* Xingqi Liu ([xqliu@cnu.edu.cn](mailto:xqliu@cnu.edu.cn))

## 14 Abstract

15 Hydroclimate changes have exerted a significant influence on the historical trajectory of ancient  
16 civilizations in arid Central Asia where the central routes of the Silk Road have been hosted. However,  
17 the climate changes at different time scales and their possible forcing mechanisms over the last  
18 millennium remain unclear due to low-resolution records. Here, we provide a continuous high-resolution  
19 humidity history in arid Central Asia over the past millennium based on the ~1.8-year high-resolution  
20 multiproxy records with good chronological control from Lake Dalongchi in the central Tianshan  
21 Mountains. Generally, the climate was dry during the Medieval Warm Period (MWP) and Current Warm  
22 Period (CWP), and wet during the Little Ice Age (LIA), which could be attributed to the influence of the  
23 North Atlantic Oscillation (NAO) and the Atlantic Multidecadal Oscillation (AMO). Furthermore, we  
24 find that the humidity oscillation was dramatic and unstable at multidecadal to century-scale, especially  
25 within the LIA. The continuous wavelet analysis and wavelet coherence show that the humidity  
26 oscillation is modulated by the Gleissberg cycle at the century-scale and by the quasi-regular period of  
27 El Niño-Southern Oscillation (ENSO) at the multidecadal scale. Our findings suggest that the effect of  
28 the solar cycle and the quasi-regular period of ENSO should be seriously evaluated for hydroclimate  
29 predictions and climate simulations in arid Central Asia in the future.

## 30 1 Introduction



31 Arid Central Asia (ACA), far away from the ocean, is not only one of the driest and largest inland  
32 regions worldwide, but also the birthplace of the far-reaching ancient civilizations that spread along the  
33 Silk Road (Li et al., 2016; Narisma et al., 2007). Scarce precipitation, intense evaporation and fragile  
34 ecosystems render this region sensitive to abrupt changes in effective humidity. Proxy records from ACA  
35 are valuable for understanding the driving factors and processes of underlying hydroclimate evolution in  
36 the inland region, which provides useful reference for human adaptation to hydroclimate changes at  
37 present and into future (Li et al., 2016), yet very few high-quality records exist over the past millennium.  
38 Several records from ACA show similar climate patterns over the past millennium, i.e., a relatively dry  
39 Medieval Warm Period (MWP) and Current Warm Period (CWP), and a wet Little Ice Age (LIA) (Chen  
40 et al., 2015; Chen et al., 2010; Chen et al., 2019a; Chen et al., 2019b). However, the climate changes at  
41 short-time scale are unclear. Additionally, some debates occur regarding the driving mechanism of  
42 natural hydroclimate evolution over the last millennium in ACA. Many studies emphasize that internal  
43 climate variability (i.e., atmosphere-sea interaction) is supposed to be more marked than external factors  
44 (e.g., solar forcing) in influencing hydroclimate changes (Chen et al., 2019a; Chen et al., 2006; Lan et  
45 al., 2019). In contrast, several paleoclimate records prefer to highlight the possible solar forcing to the  
46 humidity oscillation over the last millennium (Song et al., 2015; Zhao et al., 2009; He et al., 2013; Ling  
47 et al., 2018). These debates are largely attributed to low-resolution records or inevitable chronological  
48 uncertainties due to the old carbon effect (Chen et al., 2010).

49 Here, we present a continuous  $\sim$ 1.8-year high-resolution humidity reconstruction with good  
50 chronological control from Lake Dalongchi in the central Tianshan Mountains of ACA over the past  
51 millennium (1180-2018 CE). Low- and high-frequency signals recovered from our reconstruction offer  
52 the potential to detect climate fluctuations at decadal to centennial scales, as well as long-term changes.  
53 Then, we explore the contribution of internal climate variability and solar activity to humidity oscillations  
54 at different timescales over the past millennium.

## 55 **2 Study site**

56 Lake Dalongchi ( $83^{\circ}16'48''\sim 83^{\circ}18'15''$  E,  $42^{\circ}26'31''\sim 42^{\circ}26'58''$  N, 2400 m above sea level) located  
57 on the south slope of the central Tianshan Mountains, is an ideal location for investigating hydroclimate  
58 changes in ACA (Fig. 1a), as the lake sits in the core area of the 'westerlies dominated climatic regime  
59 (WDCR)' (Chen et al., 2019a). It is an alpine freshwater lake formed by glacial moraine damming and



60 has a mean pH of 8.03 and a salinity of 0.31 g L<sup>-1</sup>. The lake is mainly fed by the surrounding river and  
61 precipitation within the catchment and glacial meltwater from the surrounding mountains at high  
62 elevations. The lake water flows out into Lake Xiaolongchi through the underground river. The lake  
63 water from Xiaolongchi flows westwards into the Kuche River basin (Fig. 1b). Measured in July 2018,  
64 the lake covers a surface area of ~1.4 km<sup>2</sup> and has a catchment area of ~131 km<sup>2</sup>. The maximum water  
65 depth of Lake Dalongchi reaches 7.4 m in the western lake and its depth largely decreases from west to  
66 east (Fig. 1c). Alpine coniferous forests dominated by *Picea* primarily thrive on the south and west slopes  
67 of the surrounding mountains, while the north slope is dominated by shrubs. According to the records  
68 from 1958 to 2000 at Bayanbuluk Station which is located ~100 km to the northeast of Lake Dalongchi,  
69 the mean annual temperature is -4.6 °C with a July average of 10.9 °C and a January average of -26.4 °C,  
70 and the mean annual precipitation and evaporation are 270 mm and 3200 mm, respectively. The mean  
71 annual precipitation is far less than the evaporation capacity. Moreover, most of the precipitation occurs  
72 as convective rainfall from June-August (Lan et al., 2018).

### 73 **3 Materials and methods**

#### 74 **3.1 Sampling**

75 In July 2018 and August 2019, we retrieved several parallel long sediment cores from Lake  
76 Dalongchi at a maximum water depth of 7.4 m using the UWITEC platform manufactured in Austria,  
77 and several short cores using a piston gravity corer (Fig. 1c). To determine overlaps and ensure the  
78 continuity of the cores, magnetic susceptibility (MS) nondestructive scanning of all long and short  
79 sediment cores was used to obtain a 6.95m-long composite core (DLC1819) (Fig. 2). The composite core  
80 is mainly composed of clayey silt and can be divided into two lithology units from bottom to top. Unit A  
81 (695-430 cm) is mainly composed of dark or light brown clayey silt with clear lamination. Unit B (430-  
82 0 cm) has a dramatic lithological variation characterized by brown or greyish-green clayey silt and no  
83 obvious lamination (Fig. 2).

#### 84 **3.2 Laboratory analysis**

85 DLC1819 core was subsampled at 1-cm intervals. All subsamples were stored in a freezer in our  
86 laboratory at a constant temperature of 4 °C and used for MS, grain size, total organic carbon (TOC), and  
87 total nitrogen (TN) analyses. Samples for MS were dried at below 40 °C in a constant temperature air-  
88 blast drying oven and ground and packed into standard plastic boxes with a capacity of 2\*2\*2 cm<sup>3</sup>. A



89 Bartington MS2 susceptibility meter was used to measure the sample mass susceptibility. Samples used  
90 for grain size measurement were pretreated with 10-20 mL of 10% H<sub>2</sub>O<sub>2</sub> to remove organic matter and  
91 then with 10 mL of 10% HCl to remove carbonates; next, samples were rinsed with deionized water and  
92 finally treated with 10 mL 0.05 M (NaPO<sub>3</sub>)<sub>6</sub> on an ultrasonic vibrator for 10 min to promote dispersion.  
93 Grain size distributions were determined using Malvern/MS 3000 laser grain size analyzer. The samples  
94 used for TOC and TN determination were decalcified with 10% HCl and rinsed repeatedly with deionized  
95 water. Then, ~3-5 mg dried and ground samples were analyzed using the EURO EA 3000 elemental  
96 analyzer.

97 Terrestrial plant remains at different depths in DLC1819 core were used for accelerator mass  
98 spectrometry (AMS) <sup>14</sup>C measurements at Beta Analytic Inc., U.S.A. (Table 1). The uppermost sediments  
99 were used for the radiometric dating by measuring the activity of <sup>137</sup>Cs as a function of depth. The  
100 samples of the uppermost sediments at 0.5 cm intervals were dried and ground to less than 100 mesh and  
101 then loaded into the 5 mL cylindrical PVC tube. Radio-activities measurement of <sup>137</sup>Cs was measured by  
102 Spectrum Analysis System consisting of a high-purity germanium well detector produced by American  
103 EG& G Ortec Company, Ortec 919 spectrum controller, and IBM microcomputer with a 16 K channel  
104 multichannel analyzer.

## 105 **4 Results**

### 106 **4.1 Chronology**

107 A significant increase in <sup>137</sup>Cs activities occurred at approximately 71 cm, which could be attributed  
108 to the onset of rising concentrations of <sup>137</sup>Cs in the Northern Hemisphere (NH) at 1952 CE (Fig. 3a). The  
109 distinct peak at the depth of 64 cm was taken as the 1963 CE global fallout maximum (Pennington et al.,  
110 1973) (Fig. 3a). We established the age-depth model of DLC1819 based on the 2 <sup>137</sup>Cs ages and 9  
111 radiocarbon ages by the Bacon 2.2 procedure in R 3.2 software using the Bayesian method (Blaauw and  
112 Christen, 2011) (Fig. 3b). Chronology results show that DLC1819 core covers the past 840 years with an  
113 approximate average sedimentation rate of 0.9 cm/yr.

### 114 **4.2 TOC, TN, C/N, MS, Grainsize**

115 TOC and TN results show broadly similar changes and vary between 1.14% and 8.33%, and between  
116 0.09% and 0.59%, respectively (Fig. 2). C/N ratios fluctuate between 7.95 and 18.42 with an average of  
117 10.88 and the values of C/N ratios exceed 10 at the depth of 440-650 cm, 330-400 cm, 230-300 cm, and



118 130-180 cm (Fig. 2). MS values of DLC1819 core vary between 5.90 and  $41.89 \times 10^{-8} \text{ m}^3/\text{Kg}$  with an  
119 average of  $20.66 \times 10^{-8} \text{ m}^3/\text{Kg}$  (Fig. 2). The silt fraction values fluctuate from 43.64% to 88.50% with an  
120 average of 71.91% while the variation of clay fraction has an opposite trend to that of silt, and its values  
121 vary from 11.84% to 54.26% with an average of 25.97% (Fig. 2). Sand fraction only accounts for 2.43%  
122 of the total grain size on average. Generally, the higher values of the MS and silt fraction and the lower  
123 values of the clay fraction correspond to the higher C/N ratios and vice versa (Fig. 2).

#### 124 **4.3 Humidity Index reconstruction**

125 Lake Dalongchi is a typical small lake with a surface area of  $\sim 1.4 \text{ km}^2$ . The drainage basin is  
126 surrounded by high mountains and has a steep headwall. Thus, it possesses sediments that preserve a  
127 highly sensitive record of past watershed material input changes. During the humid/dry period  
128 represented by high/low lake level and enlarged/reduced lake area, exogenous materials containing  
129 magnetic minerals, coarse grain components, and terrestrial plants were poorly/easily transported to the  
130 site from which we took the core due to the long/short distance from the lakeshore and  
131 reduction/intensified erosion in the basin (Fig. 4). Terrestrial plants usually have C/N ratios of more than  
132 20 (Meyers, 1994, 2003), so the increased C/N ratios reflect the input amount of allochthonous organic  
133 matter. Thus, the high susceptibility, silt content, and C/N ratios indicate a dry climate and vice versa  
134 (Fig. 4).

135 Accordingly, multiple proxies, such as C/N ratios, MS, silt, and clay fractions, were synthetically  
136 employed to reconstruct the Humidity Index (HI) in Lake Dalongchi region over the past millennium  
137 (Fig. 5). As the high values of C/N ratios, MS, and silt contents, and low values of clay content reflect  
138 the arid climatic environment, the first three records multiplied by (-1) and clay content were normalized  
139 to a Z-score (Figs. 5b, c, d, e). Then the HI was derived from the average of the normalized standard Z-  
140 scores. Positive and negative Z-scores indicate dry and wet climatic conditions (Fig. 5a).

## 141 **5 Discussion**

### 142 **5.1 The humidity changes over the last millennium**

143 The reconstructed HI shares good consistency with the instrumental relative humidity records over  
144 the past 60 years ( $r = 0.298^*$ ) from the nearby Bayanbuluk meteorological station (Fig. 6a), verifying the  
145 reliability of the humidity reconstruction. The HI changes show that the climate was dry during the MWP  
146 (1180-1420 CE) and CWP (1920-2018 CE), and wet during the LIA (1420-1920 CE) (Fig. 6b). This



147 multi-centennial climate pattern is in agreement with the hydroclimatic patterns revealed by numerous  
148 studies in ACA (Chen et al., 2006; Song et al., 2015; Lan et al., 2018; Lan et al., 2019; Zhao et al., 2009;  
149 He et al., 2013; Ma and Edmunds, 2006; Gates et al., 2008) (Figs. 6c, d, e, f, g). Previous studies indicate  
150 the negative phase of the NAO and AMO during the LIA favors increasing precipitation in ACA (Chen  
151 et al., 2019b; Chen et al., 2015; Lan et al., 2018; Aichner et al., 2015; Chen et al., 2006; Chen et al.,  
152 2016). During the MWP, the positive phase of the NAO with enhanced pressure between the Azores High  
153 and the Icelandic Low would lead to strengthened zonal flow, and the axis of maximum moisture  
154 transport and preferred storm track extend to the north and east (Trouet et al., 2009). In contrast, the axis  
155 of maximum moisture transport and preferred storm track migrated southwards when the NAO was in a  
156 negative phase during the LIA (Hurrell, 1995). A general cold (warm) phase of the AMO corresponds to  
157 the negative (positive) NAO phase during the LIA (MWP) (Wang et al., 2017; Ortega et al., 2015),  
158 leading to a weaker (strong) upper-level jet stream intensity and further resulting in development  
159 (recession) of the through-ridge system, consequently contributing to the increased (decreased)  
160 precipitation in ACA (Chen et al., 2019b). Thus, the multi-centennial behavior in our reconstruction  
161 might be related to the influence of the NAO and AMO on hydroclimate changes during in MWP to LIA.

162 Notably, distinct from other records in ACA (Chen et al., 2006; Ma and Edmunds, 2006; Gates et  
163 al., 2008; He et al., 2013), our reconstruction shows dramatic and unstable multidecadal to century-scale  
164 climatic variability, especially within the LIA (Fig. 6b). Four wet episodes with the sharp high HI values  
165 were recorded in the 1420-1470, 1550-1600, 1650-1720, 1800-1920 CE, and three dramatic dry periods  
166 with the low HI values were recorded in the 1470-1550, 1600-1650, 1720-1800 CE during the LIA (Fig.  
167 6b). Continuous Wavelet Transform (CWT) of HI exhibits a significant century-scale dominant  
168 oscillation ranging from 88 to 157 years, which is nearly throughout the entire time series and prominent  
169 in 1450-1800 CE, as well as a strong 50~65-year multidecadal oscillation at a 95% confidence level  
170 relative to the red noise spectrum (Fig. 7a).

## 171 **5.2 The role of the Gleissberg cycle**

172 There is a strong link and inverse relationship between the HI and TSI (Fig. 7b). The HI increased  
173 significantly and reached its peak during the several grand solar minimums (Wolf, Spörer, Maunder,  
174 Dalton), whereas the humidity decreased rapidly in the maximum solar activity period (Fig. 7b). The  
175 Wavelet Coherence (WTC) spectrum between HI and TSI shows a strong correlation and anti-phase



176 pattern (Fig. 7c). Periodicities of significant coherence for HI and TSI occurred at 88 to 146 years,  
177 particularly from 1400 CE to the present. Arrows in the significant coherence spectral area point almost  
178 entirely to the left, implying the persistent negative correlation of HI and TSI (Fig. 7c). The WTC result  
179 confirms that the persistent 88-157-year cycle of HI in CWT is associated with solar activity (Figs. 7a,  
180 c). The cycle of 88-146 years should be attributed to the century-scale solar cycle of Gleissberg  
181 (Gleissberg, 1958; Gleissberg, 1965; Ogurtsov et al., 2015). Shindell et al. examined the climate response  
182 to the solar forcing at the Maunder Minimum and indicated that even relatively small solar activity might  
183 play a primary role in century-scale climate change in NH (Shindell et al., 2001). The possible solar  
184 contribution of the Gleissberg century cycle to climate changes over at least the last millennium is mainly  
185 concentrated in the North Atlantic region (Moffa-Sánchez et al., 2014; Ogurtsov et al., 2002b; Ogurtsov  
186 et al., 2002a; Ogurtsov et al., 2015). Our reconstruction provides strong evidence for negative link  
187 between the Gleissberg solar cycle and humidity changes at century timescales.

188 The sediment records from Lake Manas in ACA showed a negative relationship between  
189 temperature and moisture variation on century timescales (Song et al., 2015). Moreover, the inverse  
190 relationship between lake-level proxies and precipitation in Qaidam Basin suggested that increased  
191 evaporation rather than decreased inflow was more responsible for lowered lake levels (Zhao et al., 2009).  
192 Therefore, a solar forcing might weaken the influence of mid-latitude precipitation and play an important  
193 role in regulating effective humidity in ACA at century timescales by controlling temperature and  
194 evaporation.

### 195 **5.3 Linkage to ENSO**

196 Paleoclimatic proxies and historical records suggest that the El Niño-Southern Oscillation (ENSO)  
197 has long-term variability in amplitude and frequency on multidecadal to centennial timescales (Yeh and  
198 Kirtman, 2007; D'arrigo et al., 2005; Li et al., 2011; Mann et al., 2000). On the multi-centennial timescale  
199 (i.e., MWP to LIA), the HI and ENSO variance (Li et al., 2011) show a similar trend in amplitude changes  
200 (Fig. 7d). The amplitudes of HI and ENSO variance both show a distinctly increasing trend during the  
201 LIA and maintain a relatively high level from ~1650 to 1950 CE (Fig. 7d). This trend suggests that the  
202 relatively humid environment and unstable hydroclimate in ACA may be associated with the increase in  
203 ENSO variance amplitude (Li et al., 2011) and more frequent ENSO events (Rustic et al., 2015) during  
204 the LIA. The results here support previous studies showing that ENSO might affect hydroclimate



205 variability in ACA at multi-centennial timescales with La Niña-like (El Niño-like) conditions during the  
206 MWP (LIA) (Chen et al., 2019a; Chen et al., 2015).

207 On the multidecadal timescales, however, the WTC between the HI and ENSO variance shows a  
208 robust negative phase relationship (Fig. 7e). In particular, the WTC result shows that the HI has a similar  
209 quasi-regular cycle of ENSO variance from 82-90-yr during the MWP to 50-60-yr thereafter (Li et al.,  
210 2011), which reveals the potential modulation of these quasi-regular cycles of ENSO variance to extreme  
211 humidity oscillations at the multidecadal timescales in ACA (Fig. 7e). Daily observational precipitation  
212 and National Center for Environmental Prediction (NCEP) reanalysis data suggest that the low-level  
213 water vapor fluxes from the Indian Ocean, transported along the eastern periphery of the Tibetan Plateau,  
214 are the most important factor leading to rainstorms in ACA (Huang et al., 2017). Thus, the quasi-regular  
215 periodic variation in ENSO amplitude is likely to influence the extreme hydroclimate at multidecadal  
216 scales in ACA over the past millennium by altering the meridional circulation conditions (Huang et al.,  
217 2017). However, the mechanisms for the different timescales between the ENSO amplitude and  
218 hydroclimate changes in ACA require further exploration through high-resolution records and simulation  
219 experiments.

## 220 **6 Conclusions**

221 We present the Humidity Index (HI) in ACA over the past millennium based on the ~1.8-year high-  
222 resolution multiproxy records from Lake Dalongchi in the central Tianshan Mountains. Our results reveal  
223 dramatic and unstable multidecadal to century-scale humidity oscillations over the last millennium,  
224 especially within the LIA, which is distinct from other records of ACA. Our findings emphasize that the  
225 Gleissberg solar cycle and quasi-regular period of ENSO amplitude play critical roles in controlling the  
226 effective humidity in ACA at century and multidecadal timescales, respectively. However, high-  
227 resolution records at different time scales and climate model simulations are still needed to improve our  
228 understanding of the physical mechanisms of the links between solar irradiance and ocean-atmosphere  
229 modes and how their coupling affects moisture variation in ACA.

## 230 **Data availability**

231 The reconstructed Humidity Index in this study are submitted to the datasets of the 4TU Center for  
232 Research Data, which can be temporarily available at <https://figshare.com/s/66270515b62cb166d8c9>.

## 233 **Author contributions**





234 SF and XL conceived this study, carried out the laboratory analysis and data interpretation, and  
235 wrote the manuscript; FS and YL performed the data analysis; XM and JW participated in the retrieval  
236 of the sediment core and sampling. All authors discussed the results and commented on the manuscript.

#### 237 **Competing interests**

238 The authors declare that they have no conflict of interest.

#### 239 **Financial support**

240 This research has been supported by the National Key Research and Development Program of China  
241 (Grant No. 2018YFA0606400), the National Natural Science Foundation of China (Grant No. 41907375),  
242 and the Basic Research Program of the Institute of Hydrogeology and Environmental Geology CAGS  
243 (Grant No. SK202007).

#### 244 **References**

245 Aichner, B., Feakins, S. J., Lee, J. E., Herzschuh, U., and Liu, X.: High-resolution leaf wax carbon and  
246 hydrogen isotopic record of the late Holocene paleoclimate in arid Central Asia, *Climate of the Past*, 11,  
247 619-633, 2015.

248 Bard, E., Raisbeck, G., Yiou, F., and Jouzel, J.: Solar irradiance during the last 1200 years based on  
249 cosmogenic nuclides, *Tellus B: Chemical and Physical Meteorology*, 52, 985-992, 10.1034/j.1600-  
250 0889.2000.d01-7.x, 2000.

251 Blaauw, M. and Christen, J. A.: Flexible paleoclimate age-depth models using an autoregressive gamma  
252 process, *Bayesian Analysis*, 6, 457-474, 10.1214/ba/1339616472, 2011.

253 Chen, F., Huang, X., Zhang, J., Holmes, J. A., and Chen, J.: Humid Little Ice Age in arid central Asia  
254 documented by Bosten Lake, Xinjiang, China, *Science in China Series D: Earth Sciences*, 49, 1280-1290,  
255 10.1007/s11430-006-2027-4, 2006.

256 Chen, F., Chen, J., Holmes, J., Boomer, I., Austin, P., Gates, J. B., Wang, N., Brooks, S. J., and Zhang,  
257 J.: Moisture changes over the last millennium in arid central Asia: a review, synthesis and comparison  
258 with monsoon region, *Quaternary Science Reviews*, 29, 1055-1068, 10.1016/j.quascirev.2010.01.005,  
259 2010.

260 Chen, F., Jia, J., Chen, J., Li, G., Zhang, X., Xie, H., Xia, D., Huang, W., and An, C.: A persistent  
261 Holocene wetting trend in arid central Asia, with wettest conditions in the late Holocene, revealed by  
262 multi-proxy analyses of loess-paleosol sequences in Xinjiang, China, *Quaternary Science Reviews*, 146,



- 263 134-146, 10.1016/j.quascirev.2016.06.002, 2016.
- 264 Chen, F., Chen, J., Huang, W., Chen, S., Huang, X., Jin, L., Jia, J., Zhang, X., An, C., Zhang, J., Zhao,  
265 Y., Yu, Z., Zhang, R., Liu, J., Zhou, A., and Feng, S.: Westerlies Asia and monsoonal Asia: Spatiotemporal  
266 differences in climate change and possible mechanisms on decadal to sub-orbital timescales, Earth  
267 Science Reviews, 192, 337-354, 10.1016/j.earscirev.2019.03.005, 2019a.
- 268 Chen, J., Chen, F., Feng, S., Huang, W., Liu, J., and Zhou, A.: Hydroclimatic changes in China and  
269 surroundings during the Medieval Climate Anomaly and Little Ice Age: spatial patterns and possible  
270 mechanisms, Quaternary Science Reviews, 107, 98-111, 10.1016/j.quascirev.2014.10.012, 2015.
- 271 Chen, J., Chen, F., Zhang, E., Brooks, S. J., Zhou, A., and Zhang, J.: A 1000-year chironomid-based  
272 salinity reconstruction from varved sediments of Sugan Lake, Qaidam Basin, arid Northwest China, and  
273 its palaeoclimatic significance, Chinese Science Bulletin, 54, 3749-3759, 10.1007/s11434-009-0201-8,  
274 2009.
- 275 Chen, J., Liu, J., Zhang, X., Chen, S., Huang, W., Chen, J., Zhang, S., Zhou, A., and Chen, F.: Unstable  
276 Little Ice Age climate revealed by high-resolution proxy records from northwestern China, Climate  
277 Dynamics, 53, 1-10, 10.1007/s00382-019-04685-5, 2019b.
- 278 D'Arrigo, R., Cook, E. R., Wilson, R. J., Allan, R., and Mann, M. E.: On the variability of ENSO over  
279 the past six centuries, Geophysical Research Letters, 32, L03711, 10.1029/2004GL022055., 2005.
- 280 Gates, J. B., Edmunds, W. M., Ma, J., and Sheppard, P. R.: A 700-year history of groundwater recharge  
281 in the drylands of NW China, The Holocene, 18, 1045-1054, 10.1177/0959683608095575, 2008.
- 282 Gleissberg, W.: The eighty-year sunspot cycle, J. Br. Astron. Assoc., 68, 148-152, 1958.
- 283 Gleissberg, W.: The eighty-year sunspot cycle in auroral frequency numbers, J. Br. Astron. Assoc., 75,  
284 227-231, 1965.
- 285 Grinsted, A., Moore, J. C., and Jevejeva, S.: Application of the cross wavelet transform and wavelet  
286 coherence to geophysical time series, Nonlinear Processes in Geophysics, 11, 561-566, 10.5194/npg-11-  
287 561-2004, 2004.
- 288 He, Y., Zhao, C., Wang, Z., Wang, H., Song, M., Liu, W., and Liu, Z.: Late Holocene coupled moisture  
289 and temperature changes on the northern Tibetan Plateau, Quaternary Science Reviews, 80, 47-57,  
290 10.1016/j.quascirev.2013.08.017, 2013.
- 291 Huang, W., Chang, S.-Q., Xie, C.-L., and Zhang, Z.-P.: Moisture sources of extreme summer precipitation



- 292 events in North Xinjiang and their relationship with atmospheric circulation, *Advances in Climate*  
293 *Change Research*, 8, 12-17, 10.1016/j.accre.2017.02.001, 2017.
- 294 Hurrell, J. W.: Decadal trends in the north atlantic oscillation: regional temperatures and precipitation,  
295 *Science*, 269, 676-679, 10.1126/science.269.5224.676, 1995.
- 296 Lan, J., Xu, H., Sheng, E., Yu, K., Wu, H., Zhou, K., Yan, D., Ye, Y., and Wang, T.: Climate changes  
297 reconstructed from a glacial lake in High Central Asia over the past two millennia, *Quaternary*  
298 *International*, 487, 43-53, 10.1016/j.quaint.2017.10.035, 2018.
- 299 Lan, J., Xu, H., Yu, K., Sheng, E., Zhou, K., Wang, T., Ye, Y., Yan, D., Wu, H., Cheng, P., Abuliezi, W.,  
300 and Tan, L.: Late Holocene hydroclimatic variations and possible forcing mechanisms over the eastern  
301 Central Asia, *Science China*, 62, 1288-1301, 10.1007/s11430-018-9240-x, 2019.
- 302 Li, J., Xie, S.-P., Cook, E. R., Huang, G., D'Arrigo, R., Liu, F., Ma, J., and Zheng, X.-T.: Interdecadal  
303 modulation of El Niño amplitude during the past millennium, *Nature Climate Change*, 1, 114-118,  
304 10.1038/NCLIMATE1086, 2011.
- 305 Li, Z., Chen, Y., Wang, Y., and Li, W.: Drought promoted the disappearance of civilizations along the  
306 ancient Silk Road, *Environmental Earth Sciences*, 75, 1116, 10.1007/s12665-016-5925-6, 2016.
- 307 Ling, Y., Dai, X., Zheng, M., Sun, Q., Chu, G., Wang, H., Xie, M., and Shan, Y.: High-resolution  
308 geochemical record for the last 1100 yr from Lake Toson, northeastern Tibetan Plateau, and its climatic  
309 implications, *Quaternary International*, 487, 61-70, 10.1016/j.quaint.2017.03.067, 2018.
- 310 Ma, J. and Edmunds, W. M.: Groundwater and lake evolution in the Badain Jaran Desert ecosystem,  
311 Inner Mongolia, *Hydrogeology Journal*, 14, 1231-1243, 10.1007/s10040-006-0045-0, 2006.
- 312 Mann, M. E., Bradley, R. S., and Hughes, M. K.: Long-term variability in the El Niño/Southern  
313 Oscillation and associated teleconnections., in: *ENSO: Multiscale Variability and Global and Regional*  
314 *Impacts*, edited by: Diaz, H. F., and Markgraf, V., Cambridge University Press, Cambridge, 357-412,  
315 2000.
- 316 Meyers, P. A.: Preservation of elemental and isotopic source identification of sedimentary organic matter,  
317 *Chemical Geology*, 114, 289-302, 10.1016/0009-2541(94)90059-0, 1994.
- 318 Meyers, P. A.: Applications of organic geochemistry to paleolimnological reconstructions: a summary of  
319 examples from the Laurentian Great Lakes, *Organic Geochemistry*, 34, 261-289, 10.1016/S0146-  
320 6380(02)00168-7, 2003.



- 321 Moffa-Sánchez, P., Born, A., Hall, I. R., Thornalley, D. J. R., and Barker, S.: Solar forcing of North  
322 Atlantic surface temperature and salinity over the past millennium, *Nature Geoscience*, 7, 275-278,  
323 10.1038/NGEO2094, 2014.
- 324 Narisma, G. T., Foley, J. A., Licker, R., and Ramankutty, N.: Abrupt changes in rainfall during the  
325 twentieth century., *Geophysical Research Letters*, 34, 306-316, 10.1029/2006GL028628, 2007.
- 326 Ogurtsov, M., Lindholm, M., Jalkanen, R., and Veretenenko, S.: Evidence for the Gleissberg solar cycle  
327 at the high-latitudes of the Northern Hemisphere, *Advances in Space Research*, 55, 1285-1290,  
328 10.1016/j.asr.2014.11.031, 2015.
- 329 Ogurtsov, M. G., Nagovitsyn, Y. A., Kocharov, G. E., and Jungner, H.: Long-Period Cycles of the Sun's  
330 Activity Recorded in Direct Solar Data and Proxies, *Solar Physics*, 211, 371-394,  
331 10.1023/A:1022411209257, 2002a.
- 332 Ogurtsov, M. G., Kocharov, G. E., Lindholm, M., Meriläinen, J., Eronen, M., and Nagovitsyn, Y. A.:  
333 Evidence of Solar Variation in Tree-Ring-Based Climate Reconstructions, *Solar Physics* 205, 403-417,  
334 10.1023/A:1014277121166, 2002b.
- 335 Ortega, P., Lehner, F., Swingedouw, D., Masson-Delmotte, V., Raible, C. C., Casado, M., and Yiou, P.: A  
336 model-tested North Atlantic Oscillation reconstruction for the past millennium, *Nature*, 523, 71-74,  
337 10.1038/nature14518, 2015.
- 338 Pennington, W., Tutin, T. G., Cambary, R. S., and Fisher, E. M.: Observations on lake sediments using  
339 fallout <sup>137</sup>Cs as a tracer, *Nature*, 242, 324-326, 10.1038/242324a0, 1973.
- 340 Rustic, G. T., Koutavas, A., Marchitto, T. M., and Linsley, B. K.: Dynamical excitation of the tropical  
341 Pacific Ocean and ENSO variability by Little Ice Age cooling, *Science*, 350, 1537-1541,  
342 10.1126/science.aac9937, 2015.
- 343 Shindell, D. T., Schmidt, G. A., Mann, M. E., Rind, D., and Waple, A.: Solar Forcing of Regional Climate  
344 Change During the Maunder Minimum, *Science*, 294, 2149-2152, 10.1126/science.1064363, 2001.
- 345 Song, M., Zhou, A., Zhang, X., Zhao, C., He, Y., Yang, W., Liu, W., Li, S., and Liu, Z.: Solar imprints on  
346 Asian inland moisture fluctuations over the last millennium, *The Holocene*, 5, 1935-1943,  
347 10.1177/0959683615596839, 2015.
- 348 Trouet, V., Esper, J., Graham, N. E., Baker, A., Scourse, J. D., and Frank, D. C.: Persistent Positive North  
349 Atlantic Oscillation Mode Dominated the Medieval Climate Anomaly., *Science*, 324, 78-80,



350 10.1126/science.1166349, 2009.

351 Wang, J., Yang, B., Ljungqvist, F. C., Luterbacher, J., Osborn, Timothy J., Briffa, K. R., and Zorita, E.:

352 Internal and external forcing of multidecadal Atlantic climate variability over the past 1,200 years, *Nature*

353 *Geoscience*, 10, 512-517, 10.1038/NGEO2962, 2017.

354 Yeh, S.-W. and Kirtman, B. P.: ENSO amplitude changes due to climate change projections in different

355 coupled models, *Journal of Climate*, 20, 203-217, 10.1175/JCLI4001.1, 2007.

356 Zhao, C., Yu, Z., and Ito, E.: Possible orographic and solar controls of Late Holocene centennial-scale

357 moisture oscillations in the northeastern Tibetan Plateau, *Geophysical Research Letters*, 36, L21705,

358 10.1029/2009GL040951., 2009.

359

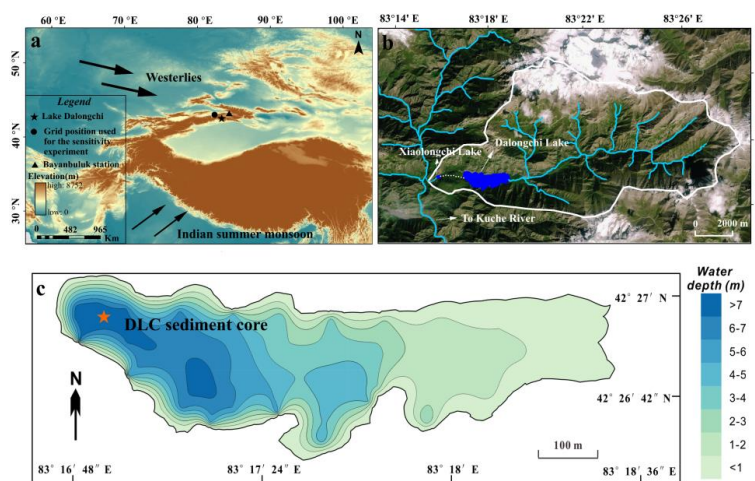
360



361 **Table 1.** Accelerator mass spectrometry (AMS)  $^{14}\text{C}$  dating results of DLC1819 core.

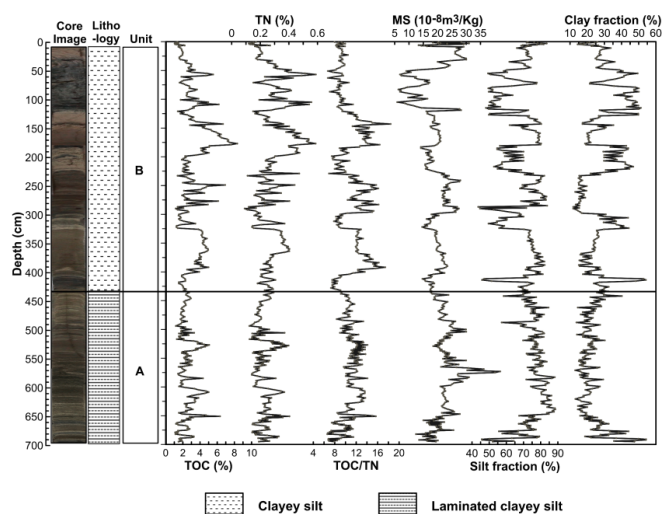
No.	Lab. No	Sample ID	Composite depth (cm)	Analyzed material	$\delta^{13}\text{C}$ (‰)	$^{14}\text{C}$ age /a BP	Calendar age/CE
1	Beta - 514897	DLC-1-1-61	69	Wood	-24.9	90+/-30	1870-1928
2	Beta - 507553	DLC-1-1-135	143	Wood	-27.4	170+/-30	1721-1818
3	Beta - 507554	DLC-1-2-82	210	Wood	-31.4	230+/-30	1635-1684
4	Beta - 507555	DLC-1-2-155	283	Wood	-26.1	340+/-30	1470-1640
5	Beta - 507556	DLC-1-3-61	324	Wood	-28.1	430+/-30	1420-1498
6	Beta - 507557	DLC-1-3-119	382	Wood	-22.3	440+/-30	1416-1490
7	Beta - 514898	DLC-1-3-131	394	Wood	-23.7	370+/-30	1446-1528
8	Beta - 514901	DLC-3-5'-37	585	Wood	-23.6	670+/-30	1274-1320
9	Beta - 542591	DLC2019-1-5-76	625	Wood	-23.1	800+/-30	1184-1275

362



363

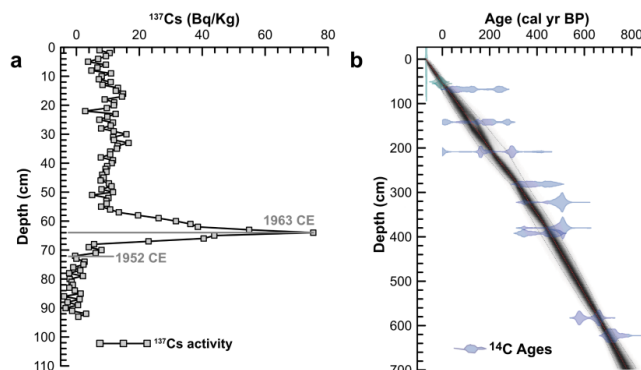
364 **Figure 1.** Maps of the study site. (a) The location of Lake Dalongchi. The map was generated by ArcMap  
 365 10.2 software (ESRI, USA, <http://www.esri.com>). (b) Watershed map of the study site. (c) Bathymetric  
 366 contour map of Lake Dalongchi with the coring site.



367

368 **Figure 2.** Sedimentary lithology and multi-proxy variation versus depth for the composite DLC1819

369 core.



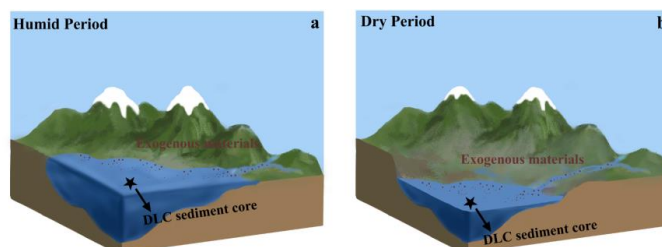
370

371 **Figure 3.** Age-depth model for the DLC1819 core of Lake Dalongchi. (a) The  $^{137}\text{Cs}$  activity versus depth

372 in the uppermost sediments. (b) Bayesian age-model for the calibrated ages. Black dots indicate the 95%

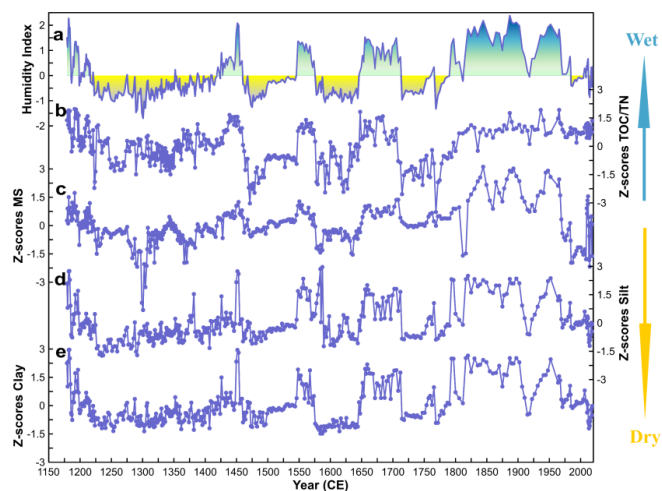
373 probability intervals of the model.

374



375

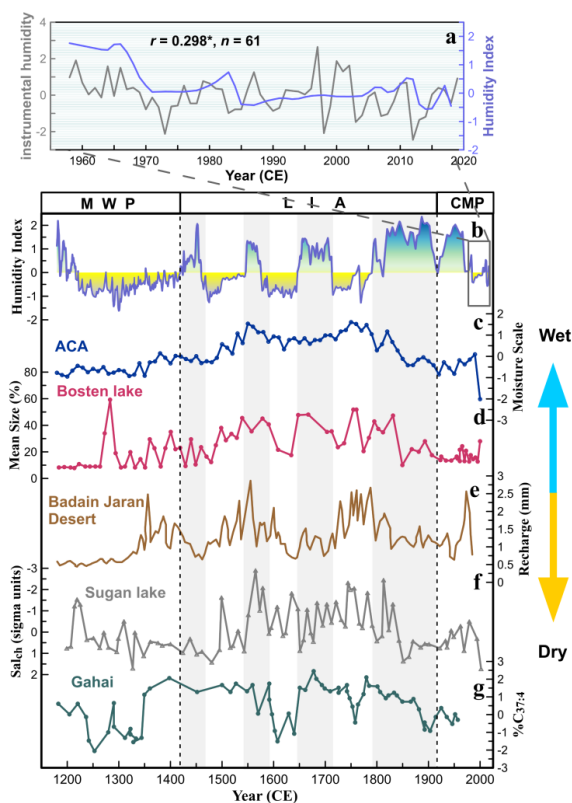
376 **Figure 4.** Cartoon schematic diagram illustrating a simple explanation of the lacustrine depositional  
377 process in Lake Dalongchi region. Lake level condition and the transport process of exogenous materials  
378 in the humid period (a) and the dry period (b).



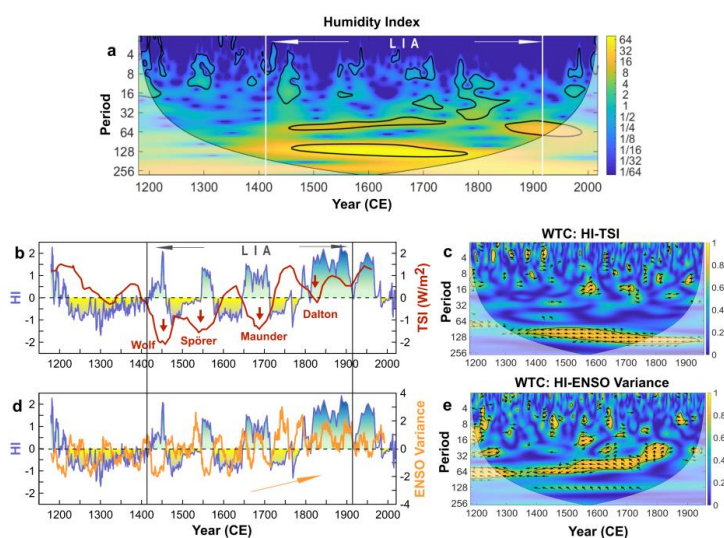
379

380 **Figure 5.** Humidity Index reconstruction (a) based on the Z-scores of total organic carbon/total nitrogen  
381 (TOC/TN) ratios (b), the Z-scores of magnetic susceptibility (MS) (c), the Z-scores of silt fraction (d),  
382 and the Z-scores of clay fraction variation (e) in the DLC1819 core in Lake Dalongchi.





383  
 384 **Figure 6.** Humidity Index (HI) of Lake Dalongchi and comparison to other records in ACA over the last  
 385 millennium. (a) Comparison between the HI (blue line) and the standardized instrumental effective  
 386 humidity recorded by Bayanbuluk meteorological station (grey line). \* represents the 0.05 significance  
 387 level. (b) The reconstructed HI for the past millennium (1180–2018 CE). (c) The synthesized moisture  
 388 curve over the last millennium in ACA (Chen et al., 2010). (d) Variations in the mean grain size along  
 389 the BST04H core in Bosten Lake (Chen et al., 2006). (e) The unsaturated recharge history in Badian  
 390 Jaran (Gates et al., 2008; Ma and Edmunds, 2006). (f) Chironomid inferred salinity (Salch) in SG03I of  
 391 Sugin Lake (Chen et al., 2009). (g) %C<sub>37:4</sub> from Lake Gahai (He et al., 2013). Light grey bars highlight  
 392 intervals of increased humidity in Lake Dalongchi during the LIA.



393  
394 **Figure 7.** The wavelet analysis of the HI and the relationship between the HI and the TSI or ENSO. (a)  
395 Continuous wavelet (CWT) power spectrum of the HI. The irregular thick black contour represents the  
396 95% confidence level against red noise and the thin curved black solid line is the cone of influence (COI)  
397 (Grinsted et al., 2004). (b) A comparison between the HI and the reconstructed total solar irradiance (TSI)  
398 (Bard et al., 2000). Wolf, Spörer, Maunder, and Dalton represent several grand solar minimums that  
399 occurred during the LIA. (c) The wavelet coherence (WTC) result between the HI and the TSI (Bard et  
400 al., 2000). (d) As (b), but for ENSO variance reconstruction (Li et al., 2011). Orange arrows represent  
401 the enhanced ENSO amplitude trend. (e) As (c), but for ENSO variance (Li et al., 2011). The 95%  
402 confidence level against red noise is shown as an irregular thick black contour. The black arrows illustrate  
403 the relative phase relationship: arrows pointing right are in-phase and those pointing left are anti-phase  
404 (Grinsted et al., 2004).  
405